UCLA
UCLA Previously Published Works

Title

An AKT3-FOXG1-reelin network underlies defective migration in human focal malformations of cortical development

Permalink

Journal

ISSN

Authors

Baek, Seung Tae
Copeland, Brett
Yun, Eun-Jin
et al.

Publication Date

DOI

Peer reviewed

An AKT3-FOXG1-reelin network underlies defective migration in human focal malformations of cortical development

Seung Tae Baek[1,2], Brett Copeland[1], Eun-Jin Yun[3], Seok-Kyu Kwon[4], Alicia Guemez-Gamboa[1], Ashleigh E Schaffer[2], Sangwoo Kim[5], Hoon-Chul Kang[1,6,7], Saera Song[1], Gary W Mathern[8,9] & Joseph G Gleeson[1,2,10]

Focal malformations of cortical development (FMCDs) account for the majority of drug-resistant pediatric epilepsy. Postzygotic somatic mutations activating the phosphatidylinositol-4,5-bisphosphate-3-kinase (PI3K)–protein kinase B (AKT)–mammalian target of rapamycin (mTOR) pathway are found in a wide range of brain diseases, including FMCDs. It remains unclear how a mutation in a small fraction of cells disrupts the architecture of the entire hemisphere. Within human FMCD-affected brain, we found that cells showing activation of the PI3K-AKT-mTOR pathway were enriched for the *AKT3*[E17K] mutation. Introducing the FMCD-causing mutation into mouse brain resulted in electrographic seizures and impaired hemispheric architecture. Mutation-expressing neural progenitors showed misexpression of reelin, which led to a non–cell autonomous migration defect in neighboring cells, due at least in part to derepression of reelin transcription in a manner dependent on the forkhead box (FOX) transcription factor FOXG1. Treatments aimed at either blocking downstream AKT signaling or inactivating reelin restored migration. These findings suggest a central AKT-FOXG1-reelin signaling pathway in FMCD and support pathway inhibitors as potential treatments or therapies for some forms of focal epilepsy.

Malformations of cortical development (MCDs) are increasingly recognized as an important cause of autism, neurodevelopmental delay and epilepsy, especially medically intractable 'catastrophic' epilepsy. Disruption of cortical development at various critical stages—such as neuronal proliferation, migration and organization—leads to characteristic MCD. FMCDs are characterized by localized cortical and subcortical lesions[1,2]. At the most severe end of the spectrum is hemimegalencephaly (HME), a clinically devastating pediatric FMCD characterized by enlargement of most or all of one entire cerebral hemisphere. Individuals with HME typically present with epilepsy, psychomotor disability and contralateral hemiparesis[3]. Most affected individuals display progressive and catastrophic epilepsy, which invariably requires radical hemispherectomy (i.e., removal of the affected cerebral hemisphere) as a surgical treatment to relieve epilepsy and to prevent further psychomotor disability.

FMCDs are characterized by cortical dyslamination and ectopic neurons in the subcortical white matter and, in the most severe form of disease, are associated with the presence of dysmorphic, cytomegalic neurons and 'balloon cells'[4,5]. The lesions are consistent with recent models of brain mosaicism[6]. Because some FMCD lesions show pathological features similar to those of tuberous sclerosis complex (TSC)-related cortical tubers (i.e., the presence of phosphorylated ribosomal protein S6 (pS6), a downstream component of mTOR activation)[3], mutations in the mTOR pathway were anticipated.

Recently, postzygotic brain-specific somatic mosaic mutations in *PIK3CA*, *AKT3* and *MTOR* were identified in FMCDs[1,7–10]. Mutations were found in 8–30% of cells and were some of the same gain-of-function activating mutations that were seen in solid malignancies, including glioblastoma multiforme (GBM). Sequencing at the single-cell level identified a mutation burden in both neural and non-neural cells, indicating that mutations occur in progenitors[11]. However, the mechanisms of disease and the potential for treatment remain poorly defined. Moreover, the mechanism by which a relatively small percentage of cells with a mutation can disrupt the organization of the entire hemisphere is mostly unknown[12].

RESULTS
Mosaic mutation is restricted to cells with mTOR activation
We focused on *AKT3*, a commonly mutated gene in FMCD[1,7,8,13]. To test whether pS6+ cells were enriched for the mosaic mutation,
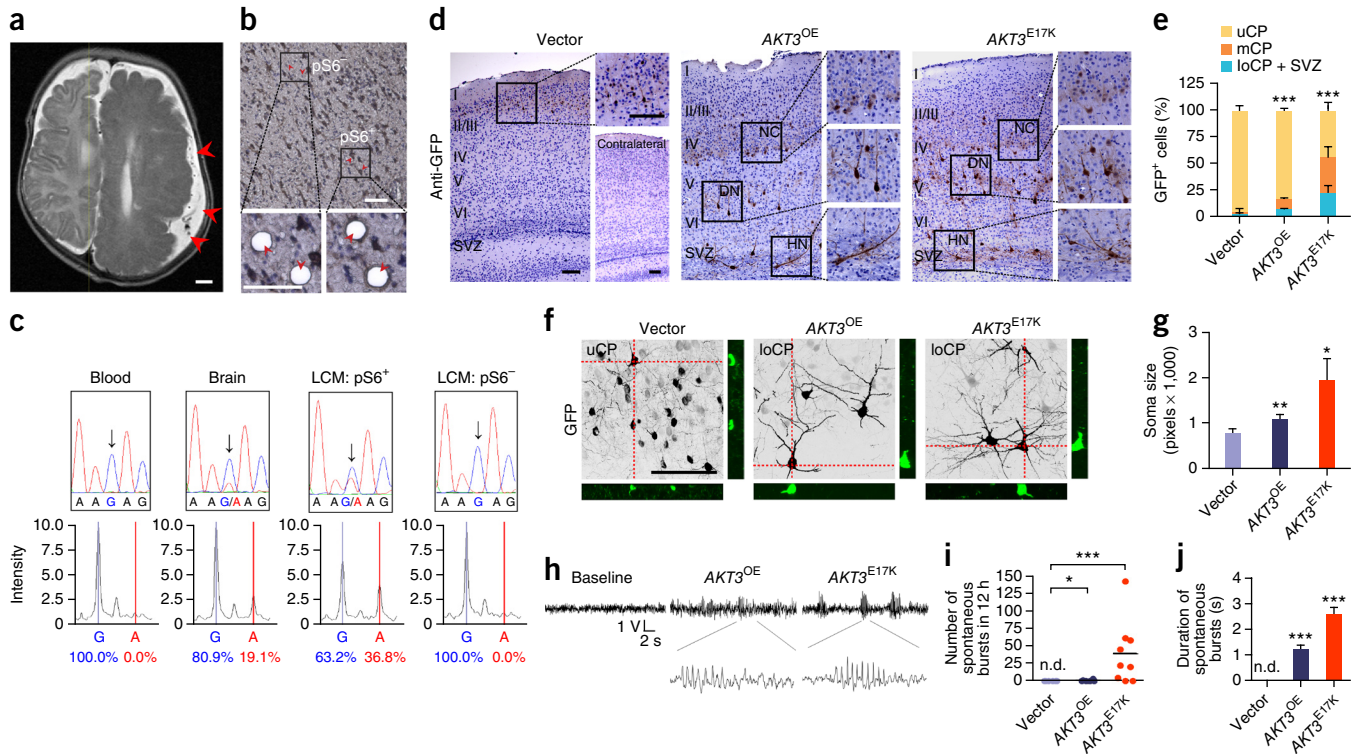
Figure 1 Modeling FMCD mutation in developing brain. (**a**) Representative presurgical axial T2 MRI of subject with hemimegalencephaly (previously reported in ref. 1) with FMCD due to somatic mosaic $AKT3^{E17K}$ mutation, with disorganization across the entire hemisphere (arrowheads) as compared to the healthy contralateral hemisphere. Scale bar, 1 cm. (**b**) Representative images of a human brain section with somatic mosaic $AKT3^{E17K}$ mutation showing laser-captured microdissection (LCM) of pS6+ or pS6− cells ($n = 5$ brain sections). Arrowheads indicate cells that were captured. Bottom images are zoomed in views of captured cells. Scale bars, 100 μm. (**c**) Capillary (Sanger) sequencing (top) and mass spectrometry (bottom) analyses of total DNA from blood, brain tissue and microdissected (LCM) hematoxylin-stained foci of pS6+ and pS6− cells ($n = 5$ brain sections). Arrows indicate the G-to-A mutation in $AKT3^{E17K}$. (**d,e**) Immunostained (for GFP) images (**d**) and quantification of GFP+ cells that were localized to uCP (layers I–IV), mCP (layer V), loCP (layer VI) or SVZ of the P20 brain sections (**e**) of mice that were electroporated in utero at E14.5 with a GFP-only control expression vector ($n = 4$) or vectors with GFP and either wild-type AKT3 ($AKT3^{OE}$, $n = 5$) or $AKT3^{E17K}$ ($n = 5$). Insets in **d** show neuronal crowding (NC), dysmorphic neurons (DN) and heterotopic neurons (HN). Contralateral side showed no structural defect. (**f,g**) Representative confocal z-stack images of 25-μm sections of a P20 mouse brain (orthogonal slice views of dashed lines are shown on the right and bottom of each image) (**f**) for quantification of cell size (**g**) (vector, $n = 4$; $AKT3^{OE}$, $n = 5$; $AKT3^{E17K}$, $n = 5$). Five nonconsecutive images per brain were analyzed for quantification. In **d,f**, scale bars, 100 μm. (**h–j**) Representative surface EEG recordings from 1-month-old mice (**h**). (**i,j**) Number (**i**) and duration (**j**) of spontaneous electroencephalographic bursts in a 12-h window (vector, $n = 4$; $AKT3^{OE}$, $n = 6$; $AKT3^{E17K}$, $n = 9$). Error bars are mean ± s.d. *$P < 0.05$; **$P < 0.01$; ***$P < 0.001$; n.d., not detected; by G-test of goodness-of-fit (**e**) or Student's t-test (**g,i,j**).

we studied a human FMCD brain tissue sample with a somatic gain-of-function mutation (c.49G>A; p.E17K—and we hereafter refer to the mutated gene as $AKT3^{E17K}$) that was present in 19.1% of the measured alleles on the basis of mass spectrometric analysis (**Fig. 1a–c**)[1]. Laser-captured microdissection of pS6+ versus pS6− neural cells was followed by PCR, capillary sequencing and single-base extension mass spectrometry to test for the mutant allele. Analysis of captured cells showed that the mutant allele was undetectable in pools of pS6− cells, whereas pS6+ cells of the same brain section were enriched for the mutation, which was detected in 36.8% of measured alleles. We conclude that pS6 is a sensitive but not specific marker for cells carrying the mutation, suggesting that activation of the pathway is relevant to the pathogenesis of disease.

Mouse model of focal malformations of cortical development

To test whether introduction of the $AKT3^{E17K}$ FMCD-associated mutation is sufficient to cause neurodevelopmental and neuropathological features, we electroporated a vector encoding $AKT3^{E17K}$, which is found in at least two persons with FMCD, into the right hemisphere of embryonic day (E) 14.5 mice. We chose this model because we could

limit the expression of AKT3 to the neural progenitors of a single hemisphere, mimicking the somatic postzygotic mosaicism found in the embryonic brains of individuals with FMCD (**Supplementary Fig. 1a**). Electroporations were timed to predominantly target neurons destined for upper cortical plate (uCP) layer II/III, the cells proposed to be most severely affected in FMCD[14,15].

Histological examinations of mouse brains at postnatal day (P) 20 revealed key features that are observed in FMCD, including neuronal heterotopias, dysmorphic neurons with enlarged soma and neuronal crowding (**Fig. 1d–g**)[3]. Whereas only 5.6% ± 3.9% of cells that were electroporated with a control vector (expressing green fluorescent protein (GFP) as a marker) failed to reach uCP layers II/III and IV, 16.3% ± 1.6% and 55.5% ± 7.0% of cells that were electroporated with human wild-type AKT3 (i.e., overexpression; hereafter referred to as $AKT3^{OE}$) or with $AKT3^{E17K}$, respectively, were misplaced in the middle cortical plate layer (mCP, layer V), the lower cortical plate layer (loCP, layer VI) or the subventricular zone (SVZ). Misplaced cells in the SVZ expressed neuronal markers (such as NeuN) but not glial markers (such as GFAP). No anatomical changes in the contralateral hemisphere were found.

Figure 2 Cellular pathology from AKT3 activation in human neural progenitor cells. (**a**,**b**) Representative images showing neural differentiation in hNPCs as assayed by MAP2 staining (green) (**a**) and quantification of MAP2$^+$ hNPCs (**b**) expressing either a *RFP*-only vector (top) or a vector with *RFP* and *AKT3*^{E17K} (bottom) after 1 d (left) or 7 d (right) in differentiation medium (DM) (*n* = 5 cultures per group). Scale bar, 100 μm. (**c**,**d**) Representative images of neurosphere assays (**c**) and quantification of migration (**d**) of sorted lentiviral-transduced hNPCs expressing either a *RFP*-only vector or a vector with *RFP* and *AKT3*^{E17K}. MAP2 (green) and DAPI (blue) staining were used to define the edge of the neurosphere (**c**, left). MAP2 (black) staining (**c**, right) was used to measure migration distance by measuring the distance of MAP2$^+$ cells from the neurosphere boundary. Dashed lines define the boundary of the neurosphere. Arrowheads show cell body position. Scale bar, 100 μm. (*n* = 15 neurospheres from five cultures per group). Error bars are mean ± s.d. *P < 0.05, **P < 0.01; by Student's *t*-test.

The most devastating pathologies of FMCD are early onset seizures, which are often medically intractable[3]. Mice electroporated with wild-type *AKT3*^{OE} or *AKT3*^{E17K} showed higher perinatal lethality (11.9% for vector control, *n* = 42; 24.3% for *AKT3*^{OE}, *n* = 37; and 67.0% for *AKT3*^{E17K}, *n* = 103), suggesting that seizures might be a cause for the increased lethality. Electroencephalogram (EEG) recordings of *AKT3*^{E17K} mice showed recurrent and unprovoked excessive electrical activity (**Fig. 1h–j**). In contrast, EEG recordings of control mice showed no such activity, whereas those of *AKT3*^{OE} mice showed only occasional bursts of shorter duration. An inflammatory response in the form of activated microglia was not apparent, suggesting that disrupted neuronal circuitry or activity was probably a cause for the observed EEG patterns.

Developmental neuropathology results from *AKT3* activation

Although clinical epilepsy may have numerous underlying cellular and molecular mechanisms, the investigation of epileptogenesis in FMCD has mostly focused on intracortical and corticothalamic projections[16]. Examination of the axonal projections of the electroporated neurons in mice showed only typical subcortical projections (data not shown). Furthermore, we found no gross changes in inhibitory neurons, as evidenced by the number or distribution of cells expressing GAD1 and GAD2 (enzymes that catalyze decarboxylation of glutamate to γ-aminobutyric acid) in the mice electroporated with *AKT3*^{E17K} as compared to those with the control vector.

We next examined whether cell fate was altered by *AKT3*^{E17K} expression. We used the layer-specific markers SATB2 (for uCP) and CTIP2 (for mCP) to examine cortical cell positioning in developing brains and confirmed defective neuronal migration at E18.5 (**Supplementary Fig. 1b**,**c**). We found no changes in the integrity of radial glia, as assessed by expression of brain lipid-binding protein (BLBP), in the electroporated regions of the developing brain (data not shown). In control vector–electroporated brains, 96% of GFP$^+$ cells were SATB2$^+$CTIP2$^-$, thus showing uCP identity. *AKT3*^{OE}- or *AKT3*^{E17K}-electroporated neurons were also predominantly SATB2$^+$CTIP2$^-$ (93% and 96%, respectively), but the cells were localized to the loCP (**Supplementary Fig. 1d**,**e**). These data suggest that despite the migration defect, birthdate-specified identity was not altered.

To test neuronal migration defects in humans, we used human neural progenitor cells (hNPCs) that were differentiated from induced pluripotent stem cells (iPSCs) from a healthy donor. We selected hNPCs because they are derived from humans, have been well studied and can express markers of both differentiating and migrating neurons
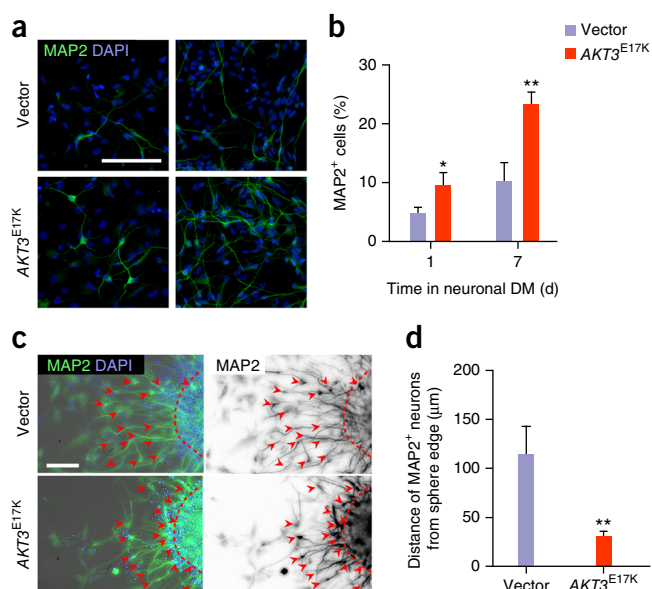
depending upon the type of media used for culture[17,18]. The hNPCs were transduced with a lentivirus expressing either red fluorescent protein (RFP) alone or *AKT3*^{E17K} with RFP and were then sorted for similar fluorescent intensities using FACS. In propagation medium, approximately 4.6% ± 1.1% of control hNPCs expressed the neuronal differentiation marker MAP2, whereas 10.3% ± 3.1% of *AKT3*^{E17K}-expressing hNPCs were MAP2$^+$. When cultured in differentiation medium, again about twice as many *AKT3*^{E17K} hNPCs were MAP2$^+$, as compared to the control hNPCs (**Fig. 2a**,**b**), suggesting that presence of the mutation leads to premature differentiation. This was confirmed in E18.5 mouse brains, in which GFP$^+$MAP2$^+$ neurons were found below the subplate in *AKT3*^{E17K}-electroporated brains but not in vector control–electroporated brains (**Supplementary Fig. 1f**).

In neurosphere migration assays, control neurons had migrated 113.8 μm ± 29.0 μm from the neurosphere edge after 2 d, whereas neurons of *AKT3*^{E17K}-expressing neurospheres were densely located near the edge and had migrated 30.9 μm ± 5.1 μm (**Fig. 2c**,**d**). Moreover, MAP2$^+$ neurons in *AKT3*^{E17K}-expressing neurospheres were often misoriented and failed to display typical migration morphology. Thus, the premature differentiation of *AKT3*^{E17K}-expressing neurons may contribute to the migration defects.

Requirement of AKT3 kinase activity

To investigate the requirement of AKT3 kinase activity in mediating neuronal migration deficits *in vivo*, we used *in utero* electroporation of human *AKT3*^{E17K} constructs that either contained or did not contain an additional K177M mutation, which renders AKT3 null for kinase activity. The kinase domain mutation in *AKT3*$^{E17K\ K177M}$ abolished not only the neuronal migration defects observed in *AKT3*^{E17K} brain sections but also the hyperphosphorylation of the downstream target pS6 (**Fig. 3a–c**), suggesting a requirement for kinase activity in cellular defects of neurons. Furthermore introducing an alanine mutation at residue S472 (*AKT3*^{S472A}), a phosphorylation site critical for AKT3 activation, also prevented pathology (**Supplementary Fig. 2a**,**b**). Conversely, a mutation that mimics phosphorylation (*AKT3*^{S472E}) and activates downstream signaling caused migration defects similar to that of *AKT3*^{E17K}. We additionally tested the effect of overexpressing human wild-type or a gain-of-function mutant of *PIK3CA* (*PIK3CA*^{OE} or *PIK3CA*^{E545K}, respectively), the gene encoding

Figure 3 AKT3 kinase activity is essential for aberrant migration phenotype. (**a**) Representative images of E18.5 mouse brain sections showing GFP (top) and pS6 staining (bottom; zoomed in views of boxed regions in top images) after *in utero* electroporation at E14.5 with *GFP*-containing vectors encoding *AKT3* variants (vector, *n* = 3; *AKT3*[OE], *n* = 3; *AKT3*[E17K], *n* = 6; *AKT3*[K177M], *n* = 5; *AKT3*[E17K K177M], *n* = 5). Scale bars, 100 μm. (**b**) Quantification of GFP+ cells in uCP, mCP and loCP regions of brain sections in **a**. (**c**) Quantification of pS6+GFP+ pixels for the images described in **a**. Error bars are mean ± s.d. ***$P < 0.001$; n.s., not significant; by G-test of goodness-of-fit (**b**) or Student's *t*-test (**c**).
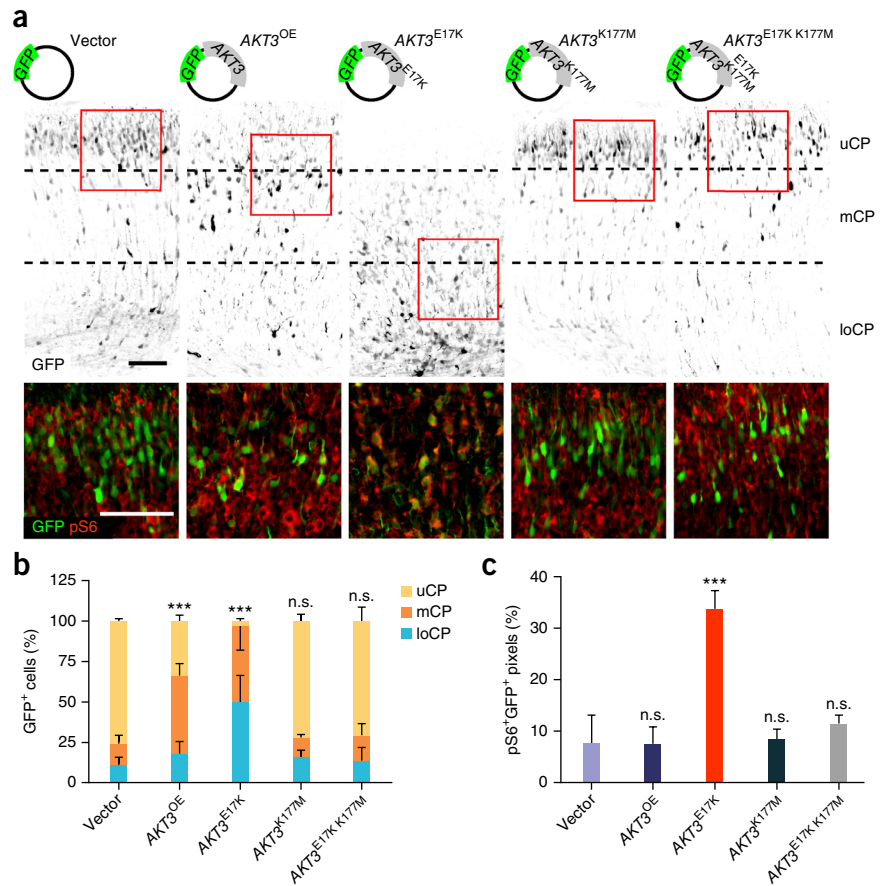
PI3K that we and others have reported to be mutated in FMCD and other segmental overgrowth syndromes[1,7], and observed neuronal migration defects and dysmorphic neurons with enlarged soma similarly to that of *AKT3*[E17K] (**Supplementary Fig. 2c–f**). Activation of PI3K in the developing cortex by inducing the expression of *PIK3CA*[H1047R], another gain-of-function mutation of *PIK3CA* found in FMCD, by using a germline knock-in allele[19] and *in utero* hemispheric electroporation of a Cre-containing plasmid, also caused similar neurodevelopmental defects (data not shown). Notably, the neuronal migration defect in brains electroporated with *PIK3CA*[E545K] was almost completely prevented by co-expression of the kinase-null *AKT3*[K177M] (**Supplementary Fig. 2c,d**), consistent with a linear signaling pathway in the etiology of FMCD. Therefore, the migration defect is not allele or gene specific but rather is due to hyperactivation of the PI3K-AKT3 pathway.

Developmental rescue of neuronal defects

To test whether inhibition of the AKT3 downstream pathway could prevent the migration defect, we administered rapamycin, a potent inhibitor of mTOR signaling, to pregnant dams for 4 d after electroporation of the *AKT3* constructs (**Supplementary Fig. 3a**). Rapamycin treatment effectively rescued AKT downstream activation in the developing cortex, as assessed by pS6 immunostaining. It also rescued, for the most part, the cortical dyslamination resulting from aberrant neuronal migration (as assessed by MAP2 immunostaining) as well as the enlarged soma size (**Fig. 4a–e** and **Supplementary Fig. 3b,c**). However, postnatal treatment with rapamycin at P1 and P3 did not restore the neuronal migration defect caused by *AKT3*[E17K] (data not shown), suggesting that there is a specific window during development for the drug to act.

Non–cell autonomous effect on migration

In *AKT3*[OE]- and *AKT3*[E17K]-electroporated hemispheres, we noticed that an ectopic layer of SATB2+ neurons in the intermediate zone (IZ) or the SVZ also included cells that were GFP− (**Supplementary Fig. 1b,e**), suggesting an effect of the mutant cells on neighboring wild-type cells. To explore potential non–cell autonomous migration defects, we performed sequential *in utero* electroporation experiments[20] of a vector expressing RFP followed by the *AKT3*[E17K]

construct that also expresses GFP, and found that *AKT3*[E17K]-expressing (i.e., RFP−GFP+) cells affected the migration of neighboring (i.e., RFP+GFP−) cells (**Fig. 5a,b**). Bromodeoxyuridine (BrdU) birthdating analysis from E14.5 injections demonstrated the presence of dual-labeled (i.e., BrdU+GFP+) ectopic *AKT3*[OE]- or *AKT3*[E17K]-expressing cells in mCP or loCP, suggesting that the misplaced cells underwent DNA synthesis concomitant with other cells that were destined for the upper cortical layers (**Supplementary Fig. 4a,b**). Additionally, no significant difference in proliferation or apoptosis rates was detected in migrating neurons (data not shown). Increased numbers of GFP− cells that were BrdU+ in the loCP of brains expressing either *AKT3*[OE] or *AKT3*[E17K] were also observed (**Supplementary Fig. 4c**). Together, these results suggest an effect of *AKT3*[E17K]-expressing cells on the migration of neighboring cells.

Functional networks underlying FMCD

The non–cell autonomous migration defect may be due to physical blockade of wild-type cells trying to migrate past mutant cells, or it may have more specific signaling mechanisms. The *AKT3*[E17K] mutation was introduced in hNPCs via lentiviral transduction using the pBOB-Switch vector, which allows for Cre-mediated recombination of the cDNA cassette (**Fig. 5c**). To obtain homogeneous *AKT3*[E17K]-expressing hNPCs, we used FACS to collect cells that were expressing RFP at similar intensities (**Supplementary Fig. 5a**), immediately isolated RNA from them and performed RNA-seq expression profiling. We identified 835 genes whose expression was significantly altered (false discovery rate–corrected $P < 0.05$) in *AKT3*[E17K]-expressing cells, as compared with empty vector–containing cells. These included several genes that were previously reported to be downstream

Figure 4 Pharmacological rescue of $AKT3^{E17K}$-induced phenotypes. (**a**) Representative images of mouse E18.5 brain sections showing localization of GFP$^+$ and MAP2$^+$ cells after *in utero* electroporation of *AKT* constructs at E14.5 followed by daily administration of rapamycin (3 μg per gram of body weight per day) to the dams (vehicle-treated: vector, $n = 3$; $AKT3^{OE}$, $n = 3$; $AKT3^{E17K}$, $n = 3$; rapamycin-treated: vector, $n = 5$; $AKT3^{OE}$, $n = 3$; $AKT3^{E17K}$, $n = 5$). Insets show presence of MAP2 in electroporated cells in the lower cortex. Arrowheads indicate rare giant neurons in rapamycin-treated embryos. Scale bars, 100 μm and 25 μm (inset). (**b**,**c**) Quantification of GFP$^+$ cells in the upper (uCP), middle (mCP) and lower (loCP) cortical plate regions (**b**) and proportion of MAP2$^+$GFP$^+$ cells in the intermediate zone (IZ) and the subventricular zone (SVZ). (**d**) Representative images used to calculate soma size of the neurons from mice electroporated with *GFP* only or with $AKT3^{OE}$ or $AKT3^{E17K}$ vectors, with or without rapamycin treatment, as shown in **a**. Tissue for analysis was harvested at E18.5. GFP immunofluorescence is shown in black. Scale bar, 100 μm. (**e**) Quantification of neuronal soma size for the groups described in **d**. Error bars are mean ± s.d. Five nonconsecutive images per brain were analyzed for quantification. $**P < 0.01$; $***P < 0.001$; n.s., not significant; by G-test of goodness-of-fit (**b**) or Student's *t*-test (**c**,**e**).


of AKT signaling—such as *CDKN2A* (encoding the tumor suppressors p16^{INK4a} and p14^{ARF}), *CDKN2B* (encoding the tumor suppressor p15^{INK4b}) and *CCND1* (encoding cyclin D1)—suggesting robust methodology.

Network analysis of the 835 genes using gene ontology (GO) enrichment analysis revealed that they could be classified into four major categories—those involved in: (i) neuronal development, (ii) migration, (iii) signaling and homeostasis and (iv) cell cycle regulation (**Fig. 5d** and **Supplementary Fig. 5b**).

Genetic rescue identifies reversible FMCD network

To determine the reversibility of the molecular changes induced by the FMCD-associated mutations, Cre recombinase was introduced by adenoviral transduction into hNPCs to remove the $AKT3^{E17K}$-*RFP* cassette. Cre recombination also removed the stop codon located 5′ to the GFP start site, thus enabling visualization of the recombined cells using GFP expression (**Supplementary Fig. 5c**). Upon Cre expression, the *AKT3* transcript level was restored to its basal level (**Fig. 5e**), suggesting efficient genetic recombination that correlated with color switching from red to green. Repeating the RNA-seq analysis identified that 275 of 835 genes (i.e., one-third) were persistently misexpressed, whereas the majority 560 genes (i.e., two-thirds) showed changes that either restored expression to wild-type levels or altered gene expression in the opposite direction.

Critical role of reelin in developmental pathogenesis

The rescue of the migration defect after mice were treated with rapamycin suggested that the pathway that was disrupted by $AKT3^{E17K}$ expression was reversible, and thus we focused on the set of genes in
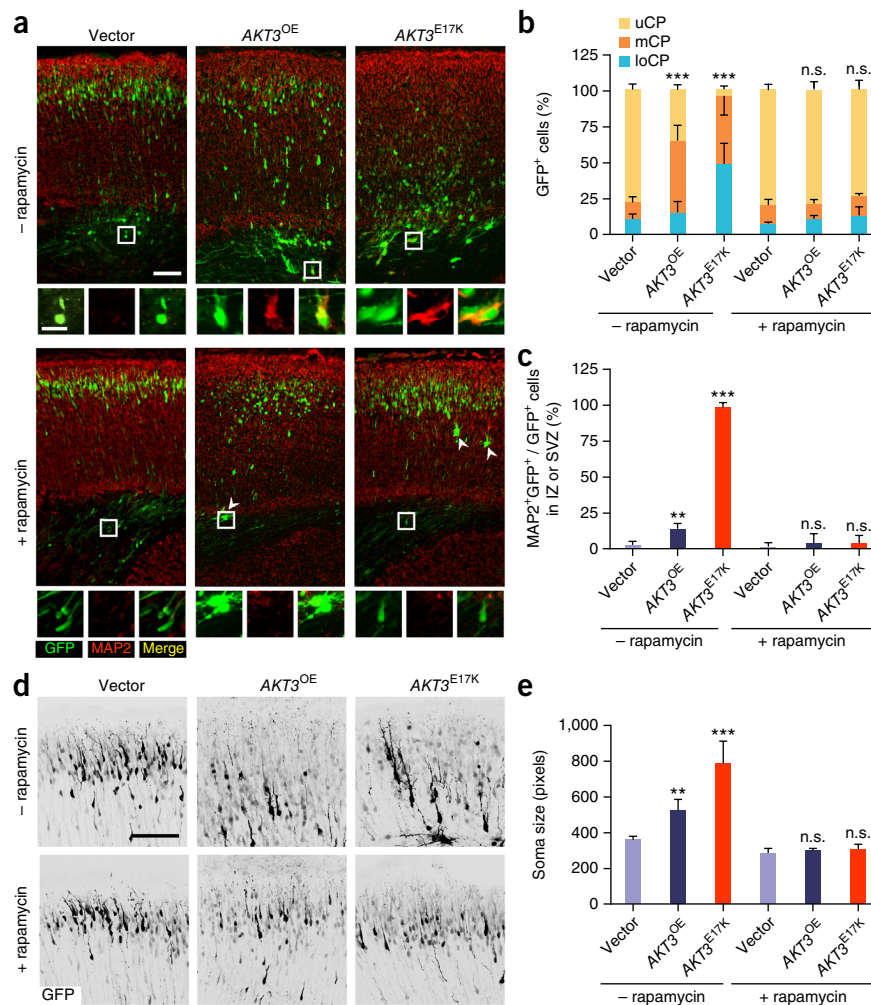
hNPCs that restored expression following Cre recombination. Among these, *RELN*, which encodes the reelin secreted glycoprotein[20] that is essential for neuronal migration and lamination during cortical development[21–24], was the most significantly affected gene ($P < 0.00005$) and was dramatically upregulated.

Loss of *RELN* leads to profound defects in neuronal positioning and dendritogenesis in human and mouse brains[25], whereas ectopic expression in migrating neurons induces neuronal ectopia[26,27]. We confirmed increased expression (~tenfold) of *RELN* in $AKT3^{E17K}$ hNPCs (**Fig. 6a**). In $AKT3^{E17K}$-expressing brains, reelin was detected in excessive amounts and localized to perisomal regions close to ectopic neurons (**Fig. 6b**). Reelin misexpression by $AKT3^{E17K}$ expression was not detected in P20 brain sections, suggesting that the pathogenic mechanisms are limited to a specific developmental window (**Supplementary Fig. 6a**). We also examined the expression of *RELN* in pS6$^+$ versus pS6$^-$ cells that were microdissected from surgically resected FMCD human brain lesions that were positive for the somatic $AKT3^{E17K}$ mutation and confirmed *RELN* expression in only one of four pools of the pS6$^+$ cells (**Supplementary Fig. 6b**). We conclude that reelin misexpression resulting from the presence of $AKT3^{E17K}$ is mostly limited to developing, rather than mature, neurons.

Reelin is initially expressed throughout in the cortical anlage at the preplate stage (E9.5), but after E11.5, its expression is mainly restricted to the Cajal-Retzius cells of the marginal zone. Therefore, we tested the degree to which defective migration in $AKT3^{E17K}$-expressing
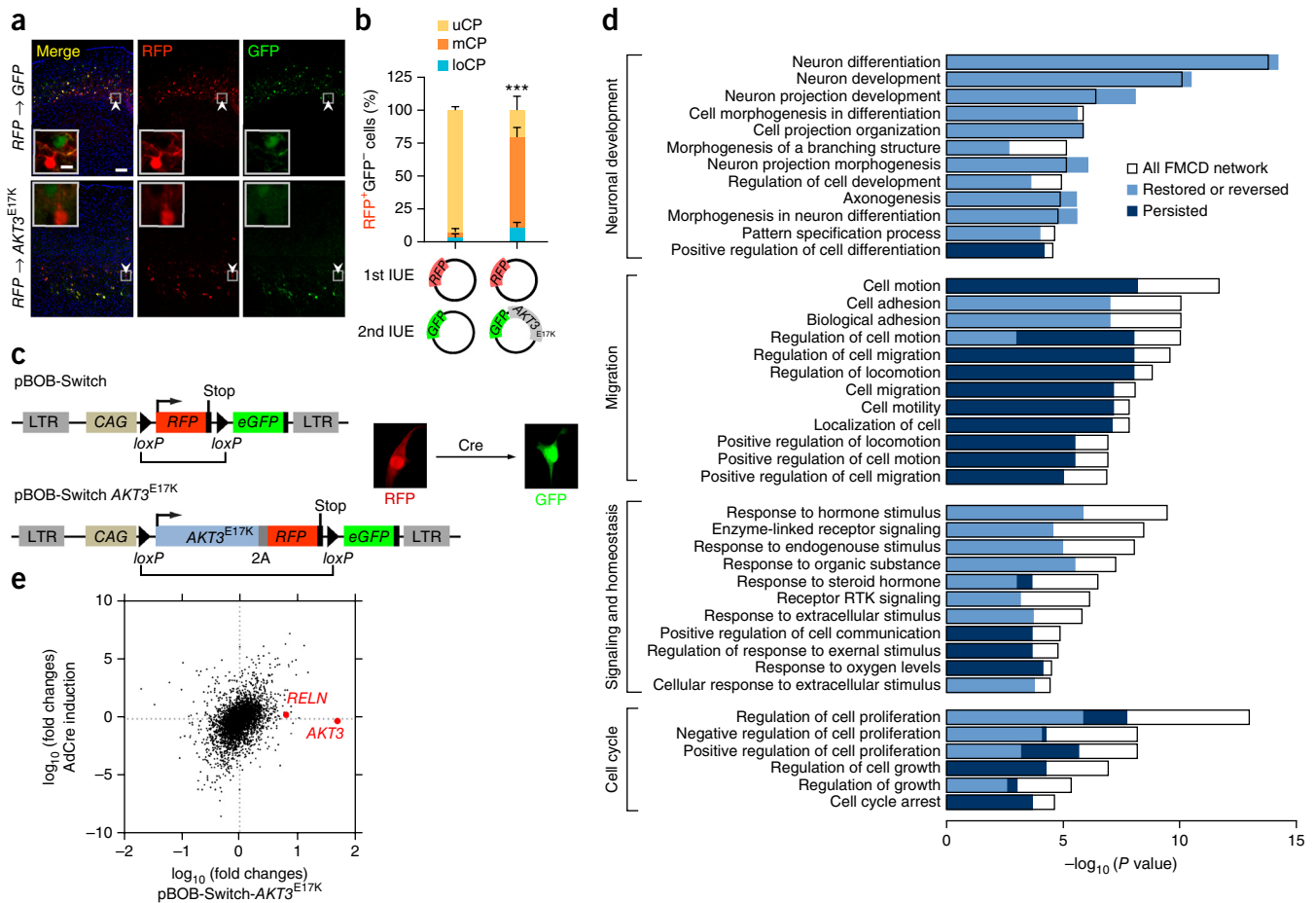
Figure 5 Genetic recombination of *AKT3*[E17K] defines reversibility of FMCD networks. (**a**) Representative images of P14 mouse brain sections after *in utero* electroporation of an RFP vector, followed by second electroporation after 15 min of a *GFP*-only vector (*n* = 5) or a vector expressing *GFP* and *AKT3*[E17K] (*n* = 3) at E14.5. Insets show nonoverlapping patterns for *RFP*- and *AKT3*[E17K]-expressing cells. Scale bars, 100 μm and 10 μm (inset). (**b**) Quantification of RFP+GFP− cells in the uCP, mCP and loCP regions in **a**. IUE, *in utero* electroporation. Error bars are mean ± s.d. ***$P < 0.001$ by G-test for goodness-of-fit. (**c**) Schematic showing the pBOB-Switch vector either without (top; as the empty-vector control) or with *AKT3*[E17K] (bottom). RFP is expressed from a bicistronic 2A sequence that encodes the self-cleaving 2A peptide and allows for stoichiometric expression of RFP and AKT3[E17K]. LTR, long terminal repeat; CAG, chicken actin promoter. The *loxP* site–flanked RFP expression cassette (along with the stop codon) is removed upon Cre recombination after adenoviral transduction, providing a color switch due to expression of GFP instead of RFP. (**d**) GO analysis identified four major enriched categories (neuronal development, migration, signaling and homeostasis, and cell cycle regulation) and several subcategories as indicated. *P* values for GO enrichment for each subcategory are shown (*x* axis). Colors indicate *P* values of the GO enrichment for the portion of the genes within each subcategory that persisted (dark blue) or that were restored (i.e., from high to background levels or from low to background levels) or reversed (i.e., from high to low levels or from low to high levels) (light blue), overlaid on each subcategory. (**e**) Comparison of mRNA levels in cells overexpressing *AKT3*[E17K] (*x* axis) versus those in cells in which *AKT3*[E17K] was genetically removed by Cre recombination (AdCre induction, *y* axis). Note that the expression of *AKT3* and *RELN* were initially elevated with *AKT3*[E17K] overexpression but were restored upon Cre recombination.

cells and its neighboring cells was due to the misexpression of reelin in ectopic regions, by using knockdown of *Reln* in cells that were electroporated with human *AKT3*[E17K]. *In utero* electroporation of *Reln* siRNA constructs into cortical progenitors alone produced no defect in migration, supporting its role in specialized Cajal-Retzius cells at this time point. However, the migration defect of *AKT3*[E17K]-expressing neurons was partially but significantly restored (*P* < 0.001) by the co-electroporation of siRNA targeting *Reln* (**Fig. 6c,d**), suggesting that overexpression of *Reln* siRNA in *AKT3*[E17K] cells leads to an autocrine or paracrine effect. To test specifically for a paracrine effect of reelin on neuronal migration, sequential electroporation of an *RFP*-containing construct followed by a mixture of a construct expressing *AKT3*[E17K] and siRNA targeting *Reln* was done such that the RFP-expressing cells should no longer be exposed to ectopic reelin

produced by the GFP+ *AKT3*[E17K]-expressing cells. This nearly fully rescued the non–cell autonomous migration defects (**Fig. 6e,f**), suggesting a central role for ectopic reelin expression in the etiology of the migration defect in *AKT3*[E17K]-expressing brains.

Reelin misregulation by activation of the AKT3-FOXG1 pathway
To investigate the mechanism by which AKT3 regulates reelin expression, we looked for commonalities in genes that were altered by *AKT3*[E17K] expression but restored after Cre recombination. We found that among the genes meeting this criterion, there was an over-representation of genes with binding sites for FOX transcription factors that were present up to 5 kb upstream of the transcription start site ($P = 1.3 \times 10^{-6}$) (**Fig. 6g**). FOX transcription factors mediate down-stream signaling from the AKT pathway. Despite the established role
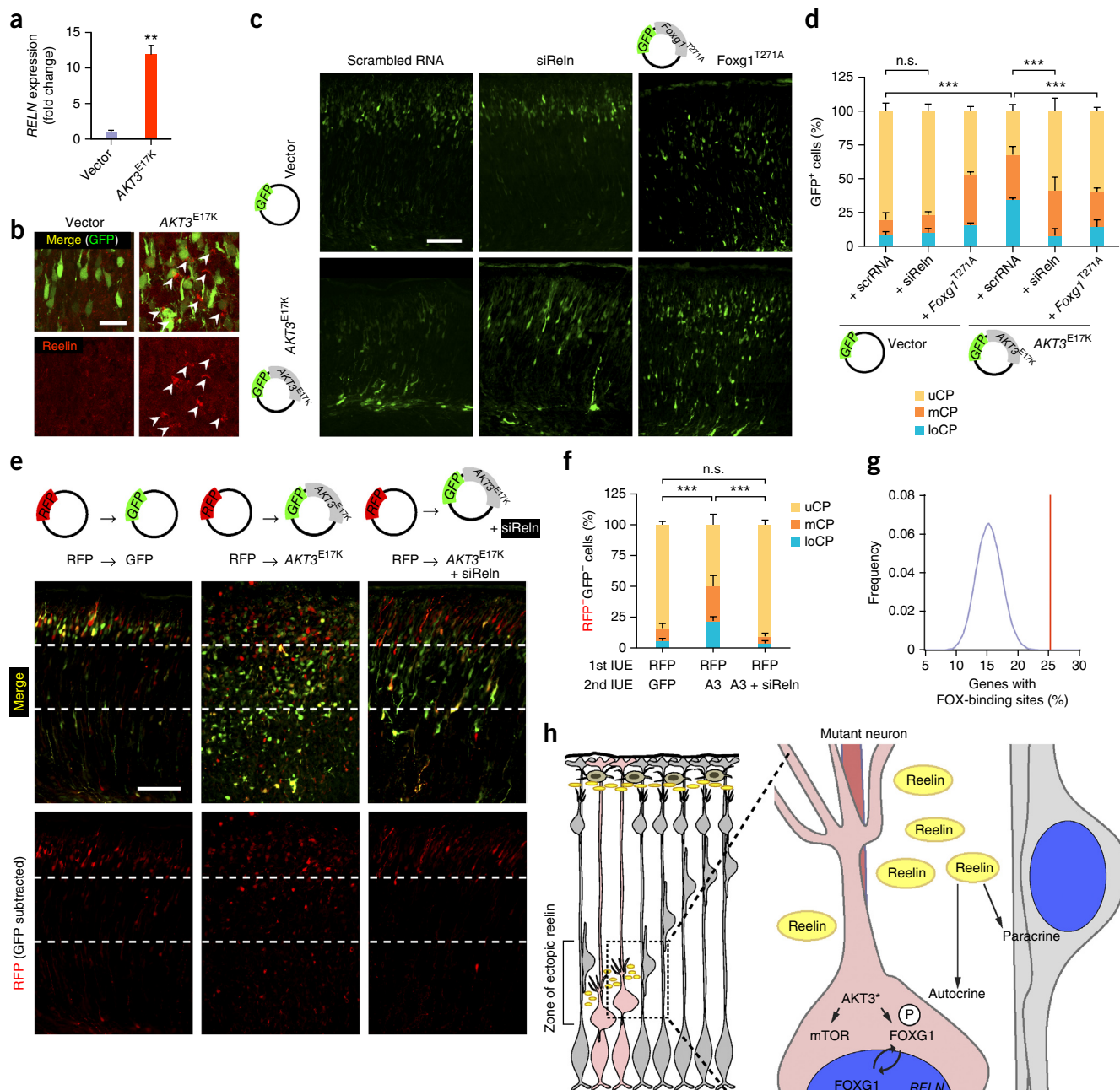
Figure 6 Neuronal migration defects rescued by *Reln* siRNA.
(**a**) Quantitative real-time PCR was performed to measure *RELN*
expression in hNPCs expressing *AKT3*[E17K] and compared to hNPCs
expressing empty vectors. Three independent experiments were quantified in triplicate.
Error bars are mean ± s.d. **$P < 0.01$; by Student's *t*-test. (**b**) Representative images of mouse
E18.5 brains showing reelin expression (red) ($n = 3$). Embryos at E14.5 were electroporated with
the indicated DNA constructs. Arrowheads indicate reelin immunostaining in the pericellular area of
ectopic neurons (intensity per pixel: 622.55 ± 45.80, as compared to 4092.77 ± 9.46 for reelin-accumulating marginal zone). Scale bar, 25 μm.
(**c**) Representative images of mouse E18.5 brains that were co-electroporated at E14.5 with indicated constructs or RNAs ($n = 3$ per group). Scale bar,
100 μm. (**d**) Localization of GFP+ neurons in **c** was quantified in each cortical region. (**e,f**) Representative images (**e**) and quantification of RFP+GFP−
cells in each region (**f**) of E18.5 mouse brain sections after *in utero* electroporation (IUE) of developing cortices with an RFP vector, followed 15 min
later by sequential electroporation of a *GFP*-only vector ($n = 3$) or a vector expressing *GFP* and *AKT3*[E17K] (A3) without ($n = 4$) or with ($n = 6$) *Reln*
siRNA. Scale bars, 100 μm. In **d,f**, error bars are mean ± s.d. ***$P < 0.001$; n.s., not significant; by G-test for goodness-of-fit. (**g**) Enrichment of
genes with FOX-binding sites. The upregulated FMCD gene set in hNPCs expressing *AKT3*[E17K] was tested for enrichment of FOX-binding sites, as
compared to a randomly selected, matched number of genes in the human genome. 10,000 iterations showed significant enrichment ($P = 1.3 \times 10^{-6}$)
of FOX-binding sites. Details in Online Methods. (**h**) Model of the effect of the *AKT3* FMCD-associated mutation on surrounding cells. Mutant cell is
pink, and surrounding cells are gray. AKT3* denotes AKT3 protein with the activating somatic mutation that leads to mTOR activation, followed by
phosphorylation and cytoplasmic sequestration of FOXG1, which then relieves repression of *RELN*. Reelin is subsequently secreted by mutant cells to
act in an autocrine (cell autonomous) and paracrine (non–cell autonomous) manner.

of the FOXO class in mediating AKT downstream effects[28], expression of constitutively active FOXO1 or FOXO3A in hNPCs did not repress *RELN* expression (data not shown).

In mice, *Foxg1* controls the morphogenesis of the telencephalon[29], and mutants show increased numbers of reelin-expressing Cajal-Retzius cells[30]. Under basal conditions, FOX factors act as transcriptional repressors, but after phosphorylation by AKT, the FOX proteins translocate to the cytoplasm, thereby inhibiting their transcriptional repressor activity[31]. Thus, we searched for conserved FOX-binding sequences and identified four potential sites (R1–R4) upstream of *RELN*. Chromatin immunoprecipitation demonstrated that FOXG1 was significantly enriched ($P < 0.001$) in two sites that have two FOX-binding sites each (**Supplementary Fig. 6c**). Next we confirmed the cytoplasmic localization of FOXG1 in hNPCs expressing *AKT3*[E17K] (**Supplementary Fig. 6d,e**). In NIH 3T3 cells, a Foxg1–GFP fusion protein predominantly localized to the nucleus; however, co-expression with *AKT3*[E17K] induced cytoplasmic translocation of the fusion protein (**Supplementary Fig. 6f,g**). Mutation of the putative T271 phosphorylation site to a nonphosphorylatable alanine (*Foxg1*[T271A]) abolished *AKT3*[E17K]-induced cytoplasmic translocation of Foxg1. Conversely, the phosphomimetic glutamic acid mutant (*Foxg1*[T271E]) increased cytoplasmic localization. Furthermore, increased *RELN* transcription in *AKT3*[E17K] hNPCs was repressed by the expression of *Foxg1*[T271A] (**Supplementary Fig. 6h**). Similar to the effects observed with *Reln* siRNA, co-electroporation of *Foxg1*[T271A] in the developing brain partially rescued the migration defects caused by *AKT3*[E17K] expression (**Fig. 6c,d**). These findings suggest that AKT3 mediates FOXG1 phosphorylation-dependent derepression of *RELN* transcription.

DISCUSSION

A major focus in neuroscience is the improved care of individuals with intractable epilepsy. The observation that the vast majority of patients undergoing surgical resection of FMCDs become seizure free and show cognitive stabilization or improvement[32] indicates that the focus for the neurocognitive defects most frequently resides within the lesion.

Here we demonstrate that postzygotic mutations that were identified in FMCDs are restricted to cells showing activation of the PI3K-AKT3 pathway and are sufficient to recapitulate the disrupted neuronal migration, excessive neuronal size, altered differentiation and epileptiform activity observed in FMCDs. We asked how somatic mutations in just a small percentage of cells could produce such severe and widespread defects in brain development. Profiling of mRNAs that were differentially expressed in *AKT3*[E17K]-expressing brains pointed to the ectopic misexpression of reelin, which we found to be due (at least in part) to the AKT3-mediated phosphorylation-dependent inactivation of Foxg1 (through its relocalization to the cytoplasm), leading to derepression of *RELN* expression in the developing brain (**Fig. 6h**).

A role for the mTOR pathway in brain development was first proposed from work in tuberous sclerosis complex (TSC)[33] and was later demonstrated through conditional removal of key regulators of the mTOR pathway, such as *Pten*, *Tsc1* and *Tsc2* (refs. 34–36). The emerging consensus is that activation of the pathway leads to neuronal hypertrophy, excessive dendritic branching and a cell type–specific effect on excitability, whereas inhibition shows the opposite effects[37–39]. Recently there has been a focus on the mTOR pathway in autism, because of both the striking autistic features displayed by persons with monogenic syndromic mTORopathies and the

evidence of mutations in the mTOR pathway in individuals with nonsyndromic forms of autism[40]. This connection is supported by animal models with a forebrain-specific deletion of *Pten* or a cerebellar-specific deletion of *Tsc1*, resulting in marked abnormalities of social behavior[41,42]. The data suggest that germline or widespread somatic mutations may result in overt structural brain defects, whereas subtle, cell type–specific or mosaic mutations may result in restricted phenotypes.

De novo heterozygous mutations in *FOXG1* are present with a congenital variant of Rett syndrome with a generalized cortical malformation[43], suggesting haploinsufficiency as a disease mechanism, whereas complete deletion in mouse results in near absence of the telencephalon[29]. Notably, whereas humans with homozygous *RELN* mutations present with a form of lissencephaly[25], *RELN* genetic variants in the 5′ untranslated region (UTR) predispose people to autistic disorder[44]. A conceptual advance from our data is that the neuronal cell migration defect observed during brain development is not due to reelin misexpression *per se* but rather to ectopic misexpression in cortical zones that are not normally exposed to reelin. Knockdown of *Reln* in developing mouse brain rescued the migration defect not just for the neighboring cells but also for the cells expressing the human *AKT3*[E17K] allele, suggesting an autocrine or paracrine effect of reelin on neuronal migration. Rapamycin rescued the non–cell autonomous migration defect—probably because of its effect on cell autonomous migration defects, thus hindering accumulation of reelin in this ectopic location. Because ectopic *Reln* misexpression was seen in the developing mouse brain but not in the mature brain, this suggests that *RELN* expression will not be a sensitive marker for cells with mTOR pathway mutations in human cortical resections.

Our results suggest two possible explanations for FMCD-related seizures in humans: cortical dyslamination due to disrupted migration or increased neuronal excitability related to morphological or signaling changes. Although cortical dyslamination can cause neuronal circuitry defects such as abnormal intracortical and corticothalamic projections that are linked to epilepsy[16,45], epileptic seizures are traditionally characterized as the synchronous neural hyperactivity arising from imbalanced excitation and inhibition[46]. On the one hand, although reelin signaling regulates dendrite growth[47] and ion channel compartmentalization that contributes to hyperpolarization-activated cation currents[48], no epileptic phenotype has been reported in mice in which reelin is either downregulated or overexpressed[49]. On the other hand, hyperactivation of the mTOR pathway can increase neuronal excitation. Thus, the data argue in favor of mTOR pathways having a larger contribution to epilepsy than reelin misexpression in the mTORopathies.

Mutations in the PI3K-AKT pathway have been recognized in brain tumors for a long time, and somatic mutations have been found in upwards of 90% of GBMs[50]. Why then do persons with FMCD with the same mutation not develop tumors? One possibility is that PI3K-AKT pathway–mediated transformation is cell cycle dependent. However, most neuroblasts are actively dividing during periods of migration, so this is unlikely to create a barrier to transformation. Another possibility is that activating mutations are not sufficient for cellular transformation in neural cells, and data certainly support cooperativity among signaling pathways, such as those involving the tumor suppressors p53 and Rb, in the induction of high-grade astrocytomas in adults[50,51]. In fact, selective activation of mTORC1 (a protein complex that controls protein synthesis) in a specific context produces microcephaly due to massive numbers of cells undergoing programmed cell death[52].

Several human syndromes such as Cowden (Online Mendelian Inheritance in Man (OMIM), 158350), Lhermitte-Duclos, CLOVES (OMIM, 612918), Proteus (OMIM, 176920) and megalencephaly (OMIM, 603387) syndromes demonstrate hamartomatous noncancerous lesions or increased organ size across the body plan, along with mutations predicted to hyperactivate the mTOR pathway[7,53,54]. Mouse models in neural progenitors demonstrate roles for the mTOR pathway in determining cellular morphology and size[35,41]. A picture of segmental overgrowth due to activating mutations is emerging[55], and *in vivo* models provide useful tools to study them[10,56]. Our finding that activating mutations in the PI3K-AKT pathway recapitulate FMCD in a mammalian model sets the stage for further mechanistic studies and development of therapies for these catastrophic disorders.

METHODS

Methods and any associated references are available in the online version of the paper.

Accession codes. RNA sequencing data have been deposited in the NCBI Sequence Read Archive with BioProject accession code SRP063581.

Note: Any Supplementary Information and Source Data files are available in the online version of the paper.

AUTHOR CONTRIBUTIONS
S.T.B. and J.G.G. designed experiments, analyzed data and wrote the manuscript. B.C. performed bioinformatics analysis of RNA-seq results. S.T.B. performed experiments. E.-J.Y. performed FOXG1 chromatin immunoprecipitation. S.-K.K. helped with *in utero* electroporation. A.G.-G., A.E.S., S.K., H.-C.K., S.S. and G.W.M. contributed key reagents and advice. J.G.G. conceived and supervised the project.

COMPETING FINANCIAL INTERESTS
The authors declare no competing financial interests.

Reprints and permissions information is available online at http://www.nature.com/reprints/index.html.

1. Lee, J.H. *et al.* De novo somatic mutations in components of the PI3K-AKT3-mTOR pathway cause hemimegalencephaly. *Nat. Genet.* **44**, 941–945 (2012).
2. Poduri, A., Evrony, G.D., Cai, X. & Walsh, C.A. Somatic mutation, genomic variation and neurological disease. *Science* **341**, 1237758 (2013).
3. Aronica, E., Becker, A.J. & Spreafico, R. Malformations of cortical development. *Brain Pathol.* **22**, 380–401 (2012).
4. Blümcke, I. *et al.* The clinicopathologic spectrum of focal cortical dysplasias: a consensus classification proposed by an *ad hoc* task force of the ILAE Diagnostic Methods Commission. *Epilepsia* **52**, 158–174 (2011).
5. Taylor, D.C., Falconer, M.A., Bruton, C.J. & Corsellis, J.A. Focal dysplasia of the cerebral cortex in epilepsy. *J. Neurol. Neurosurg. Psychiatry* **34**, 369–387 (1971).
6. McConnell, M.J. *et al.* Mosaic copy number variation in human neurons. *Science* **342**, 632–637 (2013).
7. Rivière, J.B. *et al.* De novo germline and postzygotic mutations in *AKT3, PIK3R2* and *PIK3CA* cause a spectrum of related megalencephaly syndromes. *Nat. Genet.* **44**, 934–940 (2012).
8. Poduri, A. *et al.* Somatic activation of AKT3 causes hemispheric developmental brain malformations. *Neuron* **74**, 41–48 (2012).
9. Nakashima, M. *et al.* Somatic mutations in the *MTOR* gene cause focal cortical dysplasia type IIb. *Ann. Neurol.* **78**, 375–386 (2015).
10. Lim, J.S. *et al.* Brain somatic mutations in *MTOR* cause focal cortical dysplasia type II leading to intractable epilepsy. *Nat. Med.* **21**, 395–400 (2015).
11. Evrony, G.D. *et al.* Single-neuron sequencing analysis of L1 retrotransposition and somatic mutation in the human brain. *Cell* **151**, 483–496 (2012).
12. Cai, X. *et al.* Single-cell, genome-wide sequencing identifies clonal somatic copy number variation in the human brain. *Cell Rep.* **8**, 1280–1289 (2014).
13. Conti, V. *et al.* Focal dysplasia of the cerebral cortex and infantile spasms associated with somatic 1q21.1-q44 duplication including the *AKT3* gene. *Clin. Genet.* **88**, 241–247 (2015).
14. Blümcke, I. *et al.* Malformations of cortical development and epilepsies: neuropathological findings with emphasis on focal cortical dysplasia. *Epileptic Disord.* **11**, 181–193 (2009).
15. Hadjivassiliou, G. *et al.* The application of cortical layer markers in the evaluation of cortical dysplasias in epilepsy. *Acta Neuropathol.* **120**, 517–528 (2010).
16. Cepeda, C. *et al.* Epileptogenesis in pediatric cortical dysplasia: the dysmature cerebral developmental hypothesis. *Epilepsy Behav.* **9**, 219–235 (2006).
17. Chambers, S.M. *et al.* Highly efficient neural conversion of human ES and iPS cells by dual inhibition of SMAD signaling. *Nat. Biotechnol.* **27**, 275–280 (2009).
18. Tegenge, M.A., Rockel, T.D., Fritsche, E. & Bicker, G. Nitric oxide stimulates human neural progenitor cell migration via cGMP-mediated signal transduction. *Cell. Mol. Life Sci.* **68**, 2089–2099 (2011).
19. Adams, J.R. *et al.* Cooperation between *Pik3ca* and p53 mutations in mouse mammary tumor formation. *Cancer Res.* **71**, 2706–2717 (2011).
20. D'Arcangelo, G. *et al.* Reelin is a secreted glycoprotein recognized by the CR-50 monoclonal antibody. *J. Neurosci.* **17**, 23–31 (1997).
21. Jossin, Y. & Cooper, J.A. Reelin, Rap1 and N-cadherin orient the migration of multipolar neurons in the developing neocortex. *Nat. Neurosci.* **14**, 697–703 (2011).
22. Hashimoto-Torii, K. *et al.* Interaction between reelin and Notch signaling regulates neuronal migration in the cerebral cortex. *Neuron* **60**, 273–284 (2008).
23. Sekine, K. *et al.* Reelin controls neuronal positioning by promoting cell-matrix adhesion via inside-out activation of integrin-α5β1. *Neuron* **76**, 353–369 (2012).
24. Franco, S.J., Martinez-Garay, I., Gil-Sanz, C., Harkins-Perry, S.R. & Muller, U. Reelin regulates cadherin function via Dab1/Rap1 to control neuronal migration and lamination in the neocortex. *Neuron* **69**, 482–497 (2011).
25. Hong, S.E. *et al.* Autosomal recessive lissencephaly with cerebellar hypoplasia is associated with human *RELN* mutations. *Nat. Genet.* **26**, 93–96 (2000).
26. Kubo, K. *et al.* Ectopic reelin induces neuronal aggregation with a normal birthdate-dependent 'inside-out' alignment in the developing neocortex. *J. Neurosci.* **30**, 10953–10966 (2010).
27. Sekine, K., Kubo, K.I. & Nakajima, K. How does reelin control neuronal migration and layer formation in the developing mammalian neocortex? *Neurosci. Res.* **86**, 50–58 (2014).
28. Brunet, A. *et al.* Akt promotes cell survival by phosphorylating and inhibiting a Forkhead transcription factor. *Cell* **96**, 857–868 (1999).
29. Xuan, S. *et al.* Winged helix transcription factor BF-1 is essential for the development of the cerebral hemispheres. *Neuron* **14**, 1141–1152 (1995).
30. Hanashima, C., Li, S.C., Shen, L., Lai, E. & Fishell, G. Foxg1 suppresses early cortical cell fate. *Science* **303**, 56–59 (2004).
31. Regad, T., Roth, M., Bredenkamp, N., Illing, N. & Papalopulu, N. The neural progenitor–specifying activity of FoxG1 is antagonistically regulated by CKI and FGF. *Nat. Cell Biol.* **9**, 531–540 (2007).
32. Fauser, S. *et al.* Long-term seizure outcome in 211 patients with focal cortical dysplasia. *Epilepsia* **56**, 66–76 (2015).
33. Gutmann, D.H. Tumor suppressor genes as negative growth regulators in development and differentiation. *Int. J. Dev. Biol.* **39**, 895–908 (1995).
34. Kwon, C.H. *et al.* Pten regulates neuronal soma size: a mouse model of Lhermitte-Duclos disease. *Nat. Genet.* **29**, 404–411 (2001).
35. Backman, S.A. *et al.* Deletion of *Pten* in mouse brain causes seizures, ataxia and defects in soma size resembling Lhermitte-Duclos disease. *Nat. Genet.* **29**, 396–403 (2001).
36. Feliciano, D.M., Su, T., Lopez, J., Platel, J.C. & Bordey, A. Single-cell *Tsc1* knockout during corticogenesis generates tuber-like lesions and reduces seizure threshold in mice. *J. Clin. Invest.* **121**, 1596–1607 (2011).
37. Bateup, H.S. *et al.* Excitatory-inhibitory synaptic imbalance leads to hippocampal hyperexcitability in mouse models of tuberous sclerosis. *Neuron* **78**, 510–522 (2013).
38. Tavazoie, S.F., Alvarez, V.A., Ridenour, D.A., Kwiatkowski, D.J. & Sabatini, B.L. Regulation of neuronal morphology and function by the tumor suppressors Tsc1 and Tsc2. *Nat. Neurosci.* **8**, 1727–1734 (2005).

39. Fraser, M.M. *et al. Pten* loss causes hypertrophy and increased proliferation of astrocytes *in vivo. Cancer Res.* **64**, 7773–7779 (2004).

40. Zhou, J. & Parada, L.F. PTEN signaling in autism spectrum disorders. *Curr. Opin. Neurobiol.* **22**, 873–879 (2012).

41. Kwon, C.H. *et al.* Pten regulates neuronal arborization and social interaction in mice. *Neuron* **50**, 377–388 (2006).

42. Tsai, P.T. *et al.* Autistic-like behavior and cerebellar dysfunction in Purkinje cell *Tsc1*-mutant mice. *Nature* **488**, 647–651 (2012).

43. Ariani, F. *et al. FOXG1* is responsible for the congenital variant of Rett syndrome. *Am. J. Hum. Genet.* **83**, 89–93 (2008).

44. Persico, A.M. *et al.* Reelin gene alleles and haplotypes as a factor predisposing to autistic disorder. *Mol. Psychiatry* **6**, 150–159 (2001).

45. Crunelli, V. & Leresche, N. Childhood absence epilepsy: genes, channels, neurons and networks. *Nat. Rev. Neurosci.* **3**, 371–382 (2002).

46. Truccolo, W. *et al.* Single-neuron dynamics in human focal epilepsy. *Nat. Neurosci.* **14**, 635–641 (2011).

47. Matsuki, T. *et al.* Reelin and Stk25 have opposing roles in neuronal polarization and dendritic Golgi deployment. *Cell* **143**, 826–836 (2010).

48. Kupferman, J.V. *et al.* Reelin signaling specifies the molecular identity of the pyramidal neuron distal dendritic compartment. *Cell* **158**, 1335–1347 (2014).

49. Pujadas, L. *et al.* Reelin regulates postnatal neurogenesis and enhances spine hypertrophy and long-term potentiation. *J. Neurosci.* **30**, 4636–4649 (2010).

50. Brennan, C.W. *et al.* The somatic genomic landscape of glioblastoma. *Cell* **155**, 462–477 (2013).

51. Chow, L.M. *et al.* Cooperativity within and among Pten, p53 and Rb pathways induces high-grade astrocytoma in adult brain. *Cancer Cell* **19**, 305–316 (2011).

52. Friedmann-Morvinski, D. *et al.* Dedifferentiation of neurons and astrocytes by oncogenes can induce gliomas in mice. *Science* **338**, 1080–1084 (2012).

53. Kurek, K.C. *et al.* Somatic mosaic activating mutations in *PIK3CA* cause CLOVES syndrome. *Am. J. Hum. Genet.* **90**, 1108–1115 (2012).

54. Lindhurst, M.J. *et al.* A mosaic activating mutation in *AKT1* associated with the Proteus syndrome. *N. Engl. J. Med.* **365**, 611–619 (2011).

55. Keppler-Noreuil, K.M. *et al.* Clinical delineation and natural history of the *PIK3CA*-related overgrowth spectrum. *Am. J. Med. Genet. A.* **164**, 1713–1733 (2014).

56. LoTurco, J.J. & Bai, J. The multipolar stage and disruptions in neuronal migration. *Trends Neurosci.* **29**, 407–413 (2006).

ONLINE METHODS

Animals. Timed pregnant females (C57/BL6 or CD-1) were obtained by overnight breeding with males (C57/BL6). For timed pregnancy, noon after mating was considered embryonic day (E) 0.5. Animals were obtained from Charles River Laboratories, Harlan Laboratories or Jackson Laboratory. Animal care, maintenance and experimental procedures followed the National Institutes of Health Guide for the Care and Use of Laboratory Animals[57] and the Institutional Animal Care and Use Committee (IACUC) standards at the University of California San Diego, the Rockefeller University and the Scripps Research Institute.

DNA constructs and siRNA. The pCAG-IRES-GFP (pCIG) vector was used to clone human *AKT3* or *PIK3CA*. Variants (*AKT3*[E17K], *AKT3*[K177M], *AKT3*[S472A], *AKT3*[S472E], *AKT3*[E17K S472A] and *PIK3CA*[E545K]) were generated with QuikChange II site-directed mutagenesis kit (Agilent). A PstI-digested fragment of pCIG-*AKT3*[K177M] was subcloned into PstI-digested pCIG-AKT3[E17K] to generate pCIG-*AKT3*[E17K K177M]. *AKT3*[E17K] that was linked to RFP via bicistronic 2A (which encodes self-cleaving 2A peptide for stoichiometric expression of RFP and AKT3[E17K]) was cloned into the pBOB-Switch vector to generate pBOB-Switch–AKT3[E17K]. For the Foxg1–GFP fusion protein, *Foxg1* constructs (wild-type, *Foxg1*[T271A] or *Foxg1*[T271E]) were cloned into the pCAG-GFP vector. All clones were confirmed by sequencing analysis. In *Reln* knockdown experiments, two siRNA constructs (Silencer Pre-Designed siRNA; Life Technologies; cat. no. AM16708; ID 151443 and ID 151445) were tested separately and gave similar results.

Chemicals. BrdU (Sigma) were maternally administered (100 μg per gram of body weight) by intraperitoneal injection. BrdU was dissolved in saline with NaOH (7 mM). Rapamycin (LC Labs) stock was prepared in ethanol (50 mg/ml) and diluted with vehicle (4% Tween-80; 4% polyethylene glycol 400) before injection.

***In utero* electroporation.** *In utero* electroporation was performed as described previously[58] with modifications as follows. Endotoxin-free plasmids (0.5–1 μg) plus 0.5% Fast Green (Sigma) were injected into one lateral hemisphere of E14.5 embryos. Electroporation was performed by placing the anode on the side of DNA injection and the cathode on the other side of the head to target cortical progenitors. Four pulses of 45 V for 50 ms with 500-ms intervals were used. After isolation of the brains, the contralateral hemisphere was also examined for possible anatomical changes.

Human neural progenitor cell culture and neurosphere migration assay. iPSCs derived from human primary dermal fibroblasts (American Type Culture Collection) were differentiated into neural progenitor cells (hNPCs) by standard protocol. Briefly, 3 μg of a mixture of plasmids expressing *POU5F1* (also known as *OCT3* or *OCT4*), *SOX2*, *KLF4*, *MYCL*, *LIN28A* and shRNA targeting p53 were electroporated to fibroblasts that had tested negative for mycoplasma contamination. After 7 d, cells were replated onto an irradiated CF-1 mouse embryonic fibroblast (MEF) feeder layer. The culture medium was replaced the next day with hESC-iPSC medium (Dulbecco's Modified Eagle Medium with Ham's F-12 (DMEM:F12, Thermo Fisher Scientific) supplemented with 20% KnockOut Serum Replacement (KOSR, Thermo Fisher Scientific) and 20 ng/ml basic fibroblast growth factor (bFGF, Sigma), 1× non-essential amino acids (Sigma), 110 μM 2-mercaptoethanol (Thermo Fisher Scientific)). Healthy colonies were selected for further cultivation and evaluation. After three passages, iPSCs were transferred to MEF-free plates and cultured with mTeSr medium (Stem Cell Technologies). For the generation of human neural progenitors cells, embryoid bodies (EBs) were formed by mechanical dissociation of cell clusters and plated in suspension in differentiation medium (DMEM F12, 1× N2, 1 μM dorsomorphin (Tocris), 2 μM A8301 (Tocris)) and were kept shaking at 95 r.p.m. for 7 d. EBs were then plated onto Matrigel-coated dishes and cultured with NBF medium (DMEM:F12 supplement with 0.5× B-27, 0.5× N-2 and 20 ng/ml bFGF). After 57 d, rosettes were collected and dissociated with Accutase (Millipore), and hNPCs were plated onto poly-ornithine– and laminin-coated plates with NBF medium. Medium was replaced every other day. hNPCs were characterized by immunocytochemistry for the expression of neural progenitor

cell markers (SOX2, PAX6 and nestin) and the absence of differentiated neuronal (MAP2) or glial (GFAP) markers. RNA-Seq was used to characterize expression in these cells (determined as fragments per kb of transcript sequence per million mapped fragments (FPKM) values[59,60]) of *TUBB3*, *DCX*, *SOX2*, *PAX6* and *NES* with FPKM values of 296.98 ± 8.35, 1.38 ± 0.11, 90.60 ± 2.23, 1.20 ± 0.12 and 532.20 ± 1.89, respectively. For neuronal differentiation, bFGF was withdrawn from NBF (differentiation medium). For lentiviral transduction, pBOB-Switch lentiviral vectors were cotransfected with packaging plasmids into HEK293T cells (American Type Culture Collection) that had tested negative for mycoplasma contamination using Lipofectamine LTX (Life Technologies). After 24 h, transfected cells were cultured in NBF media and viral particle–containing medium was harvested twice at 48 h and 72 h. hNPCs were cultured in virus-containing NBF medium for 24 h. Transduction efficiency was monitored by RFP expression for 48 h followed by FACS. *AKT3* overexpression and downstream activation were confirmed by western blot. For adenoviral Cre induction, 200 μl of adenovirus-containing media (~10[8] colony-forming units (c.f.u.)/ml) was added to cultures. After 8 h, cells were cultured in fresh NBF media and monitored for Cre recombination by GFP expression for 72 h followed by isolation of RFP+GFP− cells using FACS. For neurosphere migration assay, sorted hNPCs were seeded to non-coated plates containing NBF medium, with gentle agitation to generate neurospheres. Neurospheres with similar diameters were then cultured in differentiation medium for 2 d on poly-ornithine– and laminin-coated plates followed by immunostaining.

Immunohistochemistry and staining. For frozen embedding, tissues were fixed in 4% paraformaldehyde (PFA, Sigma) overnight at 4 °C with gentle rotation, immersed in 30% sucrose for cryoprotection and then embedded in Optimal Cutting Temperature (OCT) medium. Tissue sections were permeabilized with 0.1% Triton X-100 in PBS (PBT), blocked with Cas block (Life Technologies) and immunostained with antibodies against phospho-S6 (1:250; Cell Signaling; cat. no. 5364), MAP2 (1:500; Millipore; cat. no. MAB3418), reelin (1:200; Abcam; cat. no. ab78540), CTIP2 (1:500; Abcam; cat. no. ab81465), SATB2 (1:500; Abcam; ab51502) and FOXG1 (1:200, Abcam; cat. no. ab18259). For staining with BrdU antibody (1:50; BD Biosciences; cat. no. 347580), tissues were treated with HCl (2 N) before blocking. Paraffin-embedded tissues were sectioned, rehydrated and retrieved for antigen (citrated buffer, pH 6.0) before immunostaining for GFP (1:200; Rockland; cat. no. 600-106-215) followed by detection by DAB (Vector Labs). Hematoxylin (Fisher) counter-staining was performed according to the manufacturer's protocol.

Quantitative real-time PCR (qRT-PCR) and chromatin immunoprecipitation. Total RNA was extracted with PureLink RNA extraction kit or Picopure RNA extraction kit (Life Technologies) followed by cDNA synthesis with SuperScript (Life Technologies) and was subjected to qRT-PCR with CFX96 (Bio-Rad) in triplicate. Primer sequences are: *GAPDH*, forward, 5′-GGA GCG AGA TCC CTC CAA AAT-3′, reverse, 5′-GGC TGT TGT CAT ACT TCT CAT GG-3′ and *RELN*, forward, 5′-TGA GAG CCA GCC TAC AGG A-3′, reverse, 5′-TCG TTC CAC ATT CTG TAC CAA-3′. Chromatin immunoprecipitation of hNPCs was performed with IgG or FOXG1 antibodies (Abcam; cat. no. ab18259) followed by qRT-PCR. Primer sequences are: RELN-R1-forward, 5′-CCG ATT TCA GGG CCA TTG GTC-3′, RELN-R1-reverse, 5′-GCT TCT GGG CTC TTC AGG CAG-3′, RELN-R2-forward, 5′-TGG CAG TTA AGC CTC TGG GG-3′, RELN-R2-reverse, 5′-CCA AGG GGA GAC CTC TGT AAT CAC-3′, RELN-R3-forward, 5′-GGG GAC TTC CTG GGA ATT GAG G-3′, RELN-R3-reverse, 5′-GTC TGG CCA TGC TTG ATG CC-3′, RELN-R4-forward, 5′-CCC TAA TAT CCC ACC TTT CTC AGT GC-3′, RELN-R4-reverse, 5′-CAT GAG AGC AAA CCC AAT AGC AGC-3′, RELN-R4-forward, 5′-GGC TTA CTG ATC TTT AGG GTC TAT TTT TGT-3′ and RELN-R4-reverse, 5′-AAT GGT AAT AAA AGG CCA CAT GAG AGC-3′.

Mutation burden analysis using single–base pair extension. Mutation burdens were analyzed with the Sequenom MassARRAY platform as described previously[1]. Online MassARRAY Designer software (https://mysequenom.com) was used to design the primers for PCR and iPLEX single-base extension analysis. PCR and subsequent single–base pair extension reactions were performed with iPLEX Gold (Sequenom) according to the manufacturer's protocol.

Allele-specific differences in mass between extension products were detected by matrix-assisted laser desorption-ionization time-of-flight (MALDI-TOF) mass spectrometry and were analyzed by MassARRAY TyperAnalyzer software.

Laser-captured microdissection (LCM). LCM was performed with MMI CellCut Laser Microdissection system. Brain tissues were sectioned (30 μm) onto membrane slides (MMI) followed by pS6 immunostaining and hematoxylin counter-staining. Membrane with no tissue (as a negative control) or 2–20 nuclei from pS6$^+$ or pS6$^-$ cells were cut and collected to isolation caps (MMI), followed by DNA extraction. For the mutation burden analysis, genomic region covering $AKT3^{E17A}$ G-to-A mutation was amplified by nested PCR followed by capillary sequencing and single–base pair extension analysis. A minimum of seven independent samples for each condition were tested.

Imaging and quantifications. An Olympus IX51with QImaing Retiga-2000R camera was used for fluorescence imaging and a Keyence BZ-9000 for color imaging. Higher magnification images were acquired using an Olympus FV1000 confocal microscope. Analysis of images was performed with ImageJ (NIH). All images and figures were edited and created in Adobe Photoshop CS4 or Adobe Illustrator CS4.

RNA sequencing, gene ontology (GO) enrichment and FMCD network analysis. RNA was extracted and purified using the Purelink RNA kit (Life Technologies). Mature mRNA was capture by TruSeq Stranded mRNA kit (Illumina) using the standard protocol. Single-end 100-nucleotide reads were generated with Illumina HiSeq 2500 to an expected ~30 million reads per sample. RNA sequencing data have been deposited in the NCBI Sequence Read Archive with BioProject accession code SRP063581. Reads were aligned to the 1000 Genomes Project's version of GRCh37 using standard TopHat2 (http://ccb.jhu.edu/software/tophat/) v2.0.11 with single-end read options and allowing for intron-spanning reads, as defined by transcripts in Illumina's iGenomes NCBI build 37.2. Differential expression on a gene-based level was tested for with cuffdiff[61] v2.1.1 using the default option, after exclusion of one $AKT3^{E17K}$ replicate. Genes reported to be significantly differentially expressed between a pair of conditions were determined to have been so based on cuffdiff's threshold of a 0.05 false discovery rate–corrected P value. GO terms for the specified sets of genes were tested for enrichment with DAVID's functional annotation tool (http://david.abcc.ncifcrf.gov/). Cytoscape v3.1.1 with ReactomeFI plugin (http://www.cytoscape.org/) was used for functional FMCD network analysis.

Electroencephalographic (EEG) surgery. Mice were implanted under isoflurane anesthesia (1–2%), with a standard set of stainless steel screw electrodes for chronic electroencephalographic (EEG) recordings. Anesthetized animals were placed in a stereotaxic apparatus, their head hair was shaved off and the incision site was prepared with ethanol and betadine. The EEG was recorded from two bilateral electrodes inserted in the frontal bone (anteroposterior, AP = 1.0; mediolateral, ML ± 1.5) and two bilateral electrodes implanted in the parietal bone over the hippocampus (AP = −2.06; ML = 1.5), whereas a fifth electrode was placed over the cerebellum and served to ground the mouse to reduce signal artifacts. Insulated leads from these electrodes were then soldered to a miniconnector that was cemented to the skull with dental acrylic. Wounds were sutured closed, topical antibiotic ointment was applied, and mice were injected subcutaneously with the analgesic flunixin. After surgery, mice were housed in individual cages and allowed a 1-week recovery before recordings.

The ambient temperature was maintained at 25 °C ± 1.0, and a 12 h light-and-dark cycle was maintained throughout the recovery period and the subsequent experiment period. Food and water were available *ad libitum*. Once recordings were complete, the animals were anesthetized and their brains were dissected for further analysis.

Electroencephalographic analysis. EEG signals were amplified in a Grass Model 7D polygraph (Quincy, MA), filtered in a frequency range of 0.3–100 Hz and sampled at 256 Hz. The EEG signals were displayed on a computer monitor and stored with a resolution of 128 Hz in the hard drive of a computer for the off-line analysis of the vigilance states and spectral analysis, using software supplied by Kissei Comptec (Irvine, CA). The polygraphic results were analyzed semiautomatically by 15-s epochs. Epochs with artifacts in the polygraph records were discarded. Spontaneous bursts (1- to 3-s burst of spontaneous 300- to 500-mV activity) were quantified in number and duration.

Statistical analysis. The two-tailed unpaired Student's *t*-test was used to calculate P values comparing two means. G-test of goodness-of-fit was used to calculate P values comparing two mean ratios. $P < 0.05$ was considered statistically significant. No animals were excluded from the analysis. When variances between groups were found to be different, a Welch's *t*-test was used. No statistical method was used to predetermine sample size. For *in utero* electroporation, experiments were designed to include both littermate and non-littermate controls, with the exception of **Figure 1h–j**, in which mice in the control and experimental groups were not littermates. Because the animal groups were defined by electroporated DNA or RNA, no randomization was used. For **Figure 1h–j**, the investigators were blinded to group allocation during the experiment and when assessing the outcome. For **Figure 6g**, upsteam5000.fa.gz and tfbsConsSites.txt.gz were downloaded from the University of California, Santa Cruz (UCSC) Genome Browser database. These files contain the upsteam promoter sequences of all of the annotated genes in the human genome and binding sites for a number of transcription factors. The two data sets were intersected based on whether there was any overlap between the 5,000 bases upstream of each gene and the FOX-binding sites to decide for each gene whether its promoter region was associated with FOX factors. A given gene set is tested for enrichment of FOX-binding sites in its promoter by first counting the number of genes in the set whose 5′ UTRs overlap with FOX-binding sites and as a null distribution counting the number of genes that overlap for randomly selected without replacement subsets of the matched number of genes in the human genome (10,000 iterations). By using this process, an empirical P value was calculated for the significance of the enrichment for the gene list specified.

57. National Research Council. *Guide for the Care and Use of Laboratory Animals* 8th edn. (The National Academies Press, 2011).
58. Baek, S.T. *et al.* Off-target effect of doublecortin family shRNA on neuronal migration associated with endogenous microRNA dysregulation. *Neuron* **82**, 1255–1262 (2014).
59. Sarnat, H.B. Clinical neuropathology practice guide 5-2013: markers of neuronal maturation. *Clin. Neuropathol.* **32**, 340–369 (2013).
60. Zhang, Y. *et al.* An RNA-sequencing transcriptome and splicing database of glia, neurons and vascular cells of the cerebral cortex. *J. Neurosci.* **34**, 11929–11947 (2014).
61. Trapnell, C. *et al.* Transcript assembly and quantification by RNA-seq reveals unannotated transcripts and isoform switching during cell differentiation. *Nat. Biotechnol.* **28**, 511–515 (2010).